Int J Thermophys (2010) 31:1310–1346
DOI 10.1007/s10765-010-0722-z

Acoustic Resonator Experiments at the Triple Point of Water: First Results for the Boltzmann Constant and Remaining Challenges

Gavin Sutton · Robin Underwood · Laurent Pitre · Michael de Podesta · Staf Valkiers

Received: 2 November 2009 / Accepted: 4 March 2010 / Published online: 29 May 2010

Abstract We report on two sets of isothermal acoustic measurements made with argon close to the triple point of water using a 50 mm radius, thin-walled, diamond-turned quasisphere. Our two isotherms yielded values for the Boltzmann constant, k_B, which differ by 0.9 parts in 10^6, and have an average value of $k_B = (1.380\ 649\ 6 \pm 0.000\ 004\ 3) \times 10^{-23} J \cdot K^{-1}$. The relative uncertainty is 3.1 parts in 10^6, and the average value is 0.58 parts in 10^6 below the 2006 CODATA value (Mohr et al. Rev Mod Phys 80:633, 2008), and so the values are consistent within their combined ($k = 1$) uncertainties.

Keywords Acoustic resonance · Boltzmann constant · Kelvin redefinition · Microwave resonance · Quasi-sphere

1 Introduction

After studying a large number of alternatives, NPL decided that the best chance of determining a value of k_B with an uncertainty below 1 part in 10^6 was through an accurate determination of the speed of sound in a noble gas. This view was supported by Felmuth et al. [2] in their review of available methods. In choosing this technique, we are building on foundations established over two decades by Moldover et al. [3,4],

G. Sutton · R. Underwood · M. de Podesta (✉)
NPL, Teddington TW11 0LW, UK
e-mail: michael.depodesta@npl.co.uk

L. Pitre
LNE-INM/Cnam, 61 Rue du Landy, 93210 La Plaine-Saint-Denis, Paris, France

S. Valkiers
IRMM, Retieseweg 111, 2440 Geel, Belgium

and by several other researchers, notably Pitre and Moldover [5], Gavioso et al. [6], Mehl [7–11], and Oxborrow [12].

At NPL, we have begun construction of an apparatus to determine k_B with an uncertainty below 1 part in 10^6 in 2010, and, here, we report preliminary measurements made during the period from January 2009 to May 2009. The experiments were conducted using a copper quasisphere (TCU1v4) borrowed from the *Laboratoire National d'Essais* (LNE) in Paris. The sphere had an unusually thin wall designed to enhance the effect of interactions between the acoustic resonances and shell vibrations. Two determinations of k_B were made with the sphere supported differently to examine the effects of the shell interaction.

The structure of this article is as follows. In §2, we describe the experimental arrangement and procedure. In §3, we describe the analysis of the data and the steps used to deduce a value of k_B. In §4, we consider the prospects for reducing our measurement uncertainty to below 1 part in 10^6.

2 Experimental Details

2.1 The Sphere: TCU1v3

The copper quasi-sphere (Fig. 1) was originally manufactured using conventional workshop technique, but was re-machined using diamond-turning techniques by *Nanoshape* SA [13]. Diamond-turning allows very precise manufacturing to form and results in a very low surface roughness, typically described by a standard deviation $R_a \sim 5$ nm. Most of the inner surface was mirror-like except for regions near the flange, which appeared 'clouded,' presumably due to micron-level vibrations during manufacture, or possibly damage by swarf. The design form of the internal surface was a triaxial ellipsoid described by

$$\frac{x^2}{\left[a^2\right]} + \frac{y^2}{\left[a\,(1+\varepsilon_1)\right]^2} + \frac{z^2}{\left[a\,(1+\varepsilon_2)\right]^2} = 1 \tag{1}$$

with design values of $a = 50$ mm and ε_1 and ε_2 of 0.001 and 0.0005, respectively. This results in principal radii of 50.00 mm, 50.05 mm, and 50.025 mm. Coordinate measuring machine (CMM) data confirmed that the internal surface conformed closely to this form with the exception that 20 μm had been removed in error from one flange. Over most of its surface, the shell was 5 mm thick, one half the normal thickness of resonators used for acoustic thermometry.

2.2 General Arrangement

Two complete isotherms were measured close to 273.16 K while decreasing the pressure from 600 kPa to 50 kPa. Figure 2 shows the sphere in its two mounting configurations. For the first isotherm (referred to as 'fixed'), the sphere was mounted rigidly at its base to a stainless steel post of diameter 38 mm and length 100 mm. For the

Fig. 1 TCU1v3—thin shell diamond-turned 0.5-l quasi-sphere

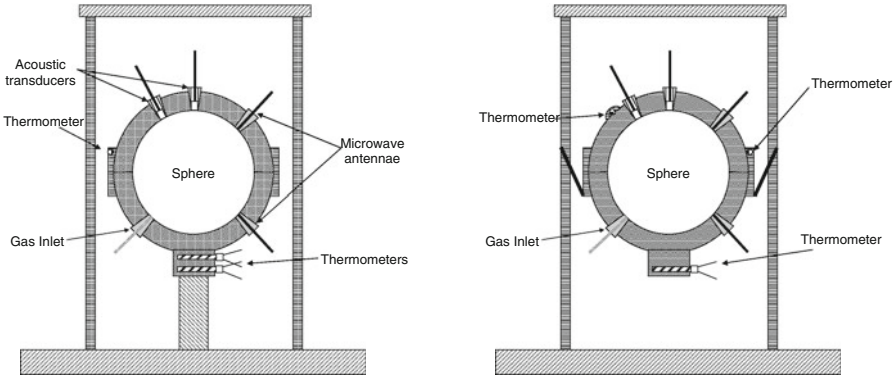

Fig. 2 The sphere in the two measurement configurations 'Fixed' and 'Hung'

second isotherm (referred to as 'hung'), the sphere was hung from its equator by three lengths of wire. Our aim in using these two mounting techniques was to measure and characterise two distinct shell corrections.

Primitive temperature control of the sphere was achieved by immersing the pressure vessel in a large dewar containing a mixture of water and ethylene glycol (Fig. 3) and use of a re-circulating heater/chiller system. The temperature drifted steadily during the isotherms (Fig. 4) by 70 mK for the 'hung' isotherm and 30 mK for the fixed isotherm. Although the drift was larger than we anticipated, a correction has been applied (§3.8), and a component in the uncertainty budget has been added to allow for this.

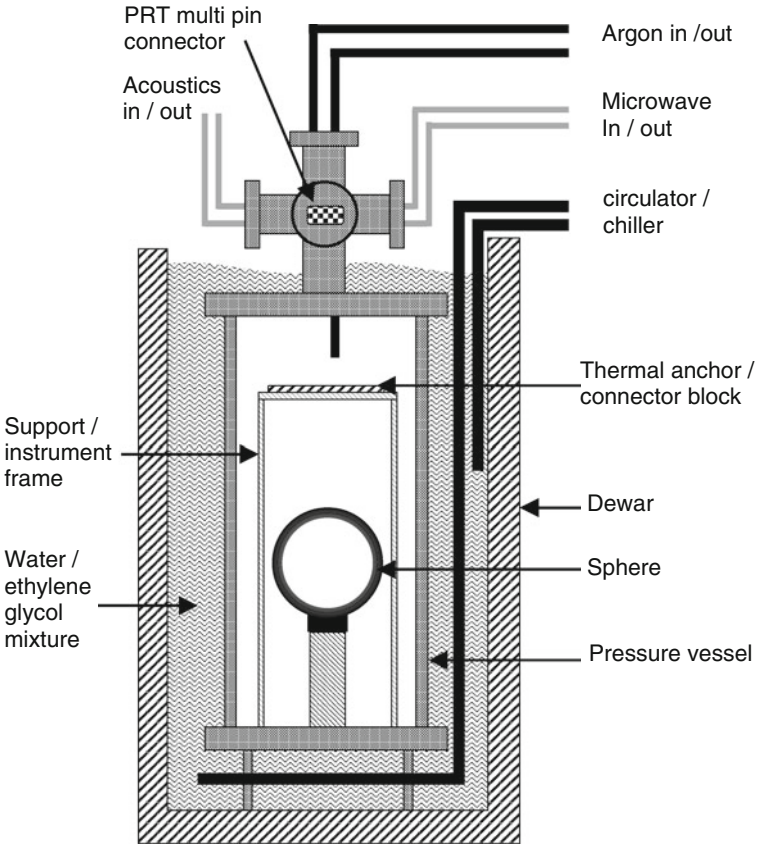

Fig. 3 Schematic diagram of the sphere and pressure vessel immersed in the dewar

Fig. 4 The difference in temperature from the triple point of water during the two isotherms. Each isotherm took approximately 5 days to complete

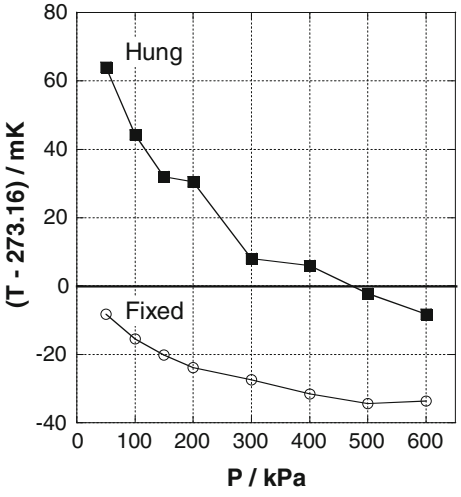

2.3 Thermometry

Three Tinsley Type 5187L standard capsule platinum resistance thermometers (cSPRTs) [14] were mounted onto the sphere. In the 'fixed' experiment, two thermometers were mounted in holes in the base of the sphere, and the third one was placed at the equator. In the 'hung' experiment, thermometers were mounted in holes in the base, along the equator and near to the top of the sphere. An ASL F18 resistance bridge [15] was used to measure the ratio of the thermometer resistance to that of a temperature-controlled 100 Ω standard resistor. Prior to the measurements, the thermometers were calibrated at the triple point of water and at the gallium melting point. Readings were corrected to zero measurement current. The calibration uncertainty was 0.5 mK; however, the uncertainty close to the triple point of water is expected to be much less. Self-heating tests where performed with the thermometers in situ, and the measurements were also corrected to zero measurement current. With all other electronics switched off, the temperature difference between the thermometers was less than ±0.1 mK which is consistent with expected calibration uncertainty. However, when the acoustic pre-amplifier (Type GRAS 26AC [16]) was switched on, a temperature gradient was apparent varying from 0.6 mK at 600 kPa to 1.4 mK at 50 kPa. After considering different schemes for compensation of this gradient, we simply took the temperature of the equatorial thermometer to represent the temperature of the sphere in all calculations in both isotherms and included a specific uncertainty component to account for the gradient.

2.4 Gas Handling

A schematic diagram of the gas-handling scheme is shown in Fig. 6. The source argon gas was supplied with a built-in purifier (BIP) consisting of a cartridge of molecular sieve. This was connected through all-metal regulators to a manifold manufactured from internally electro-polished stainless steel pipework. The pipework was not baked, but instead gas was passed through the system for one week prior to measurements. Parts of the manifold were thermally insulated to minimise pressure fluctuations resulting from laboratory temperature changes. The gas manifold allows many routing options, but typically involves passage through two point-of-use gas purifiers (SAES Model GC50 [17]) and a mass flow controller before entry to the sphere. Gas samples for analysis were captured in 100 ml bottles and sent to the *Institute for Reference Material and Measurements* (IRMM) for isotopic and purity analysis by gas mass spectrometry.

Flow and pressure control were achieved using mass flow controllers (MFCs) at the inlet and outlet of the sphere. The outlet MFC was set to maintain a given flow rate through the system. The flow rate was 50 standard cubic centimeters per minute (SCCM) during the 'fixed' isotherm, but was reduced to 5 SCCM during the 'hung' isotherm to improve pressure regulation. The inlet MFC was controlled to maintain the required pressure as indicated by *Druck DPI-150* [18] pressure meters. For the 'fixed' isotherm, pressure regulation was within 1.5 Pa of the set pressure, but for the 'hung' isotherm, the fluctuations were reduced to less than 0.3 Pa. A flow-dependent

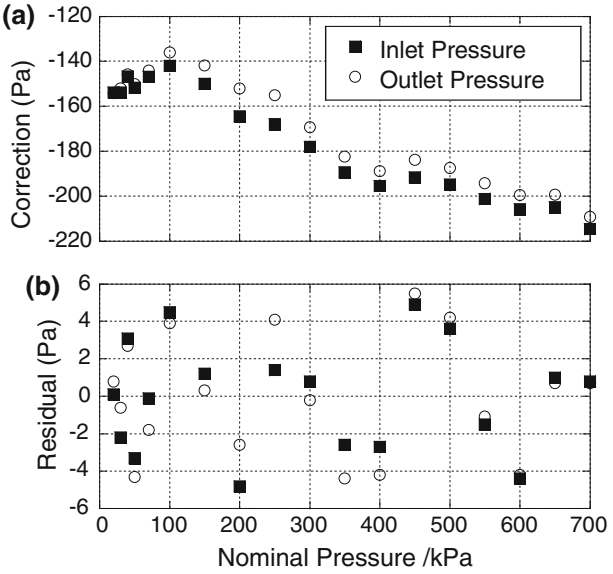

Fig. 5 (**a**) The calibration correction required for the pressure meters and (**b**) The residuals of a fit to the calibration data

correction was applied to the measured outlet pressure to determine the pressure inside the sphere. A flexible resistance heater was wrapped around the 'equator' of the sphere to counteract the temperature drop when the pressure was reduced.

In early testing, prior to acquiring data for the two isotherms, we noticed an offset on the pressure meters when exposed to vacuum pressure, and we corrected for this. However, for organizational reasons, the *Druck* DPI 150 pressure meters were only fully calibrated *after* the experiment and analysis had been completed. Significant errors were uncovered (Fig. 5). The two meters behaved similarly and had errors of approximately 150 Pa at 50 kPa (0.3 %), rising to 200 Pa at 600 kPa (0.03 %). Inadvertently, the offset we had applied had actually made the situation worse rather than better. Type testing of the meters indicated that their calibrations are stable, and so we expect the calibration to have been valid during the isotherms. After calibration, the residuals of a fit to the calibrated points were less than ± 5 Pa. Overall, the uncertainty in P is approximately 10 Pa at $k = 1$ across the entire range.

Using the corrected pressure data significantly affected our estimate of the thermal boundary layer §3.2 and duct correction §3.2. The entire analysis was repeated from the start with corrected pressure values, and it is this second analysis that is reported in §3. Also included in this second analysis was a thermo-molecular correction for the height difference (1.8 m) and temperature difference (20 °C) between the meters and the sphere. At this point, we note that despite the very significant pressure errors in the initial analysis (0.4 % at 50 kPa including our incorrect offset), the inferred value of k_B shifted by only 0.1 part in 10^6. This gives us confidence in the robustness of our estimate and the conservative nature of our uncertainty analysis.

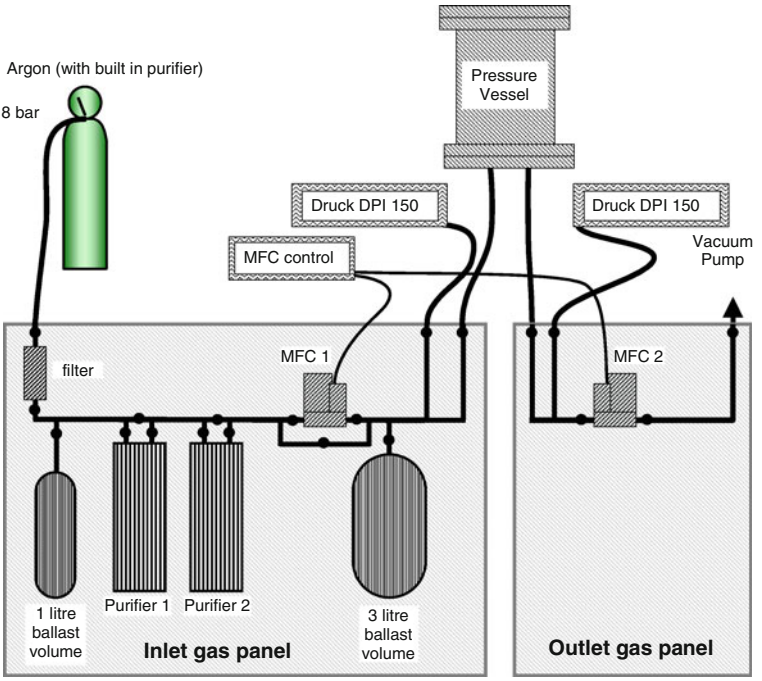

Fig. 6 Gas handling system

The gas inlet comprises a 6 m length of stainless steel tubing (internal radius 0.572 mm) wrapped around the equator of the sphere to improve thermalization of the gas. This is joined to a 100 mm tube (internal radius 0.254 mm) just prior to entering the sphere. The gas leaves the sphere via a 50 mm long tube (internal radius 0.381 mm) which vents to the pressure vessel (volume 12 L).

2.5 Argon Isotopic Analysis and Chemical Purity

The gas used for the 'fixed' experiment was *Air Products BIP+* argon, and the gas used for the 'hung' experiment was *Air Products BIP* argon. The '+' indicates a lower concentration of impurities, mainly hydrocarbons [19]

Table 1 shows a summary of the isotopic composition as measured at IRMM using a specially constructed isotope ratio mass spectrometer [20–25]. Surprisingly, the molar mass was higher by 3.77(21) parts in 10^6 for the argon used in the hung isotherm. Comparison with other analyses shows that the 'fixed' isotherm had an anomalously enhanced isotope ratio of ^{38}Ar to ^{40}Ar—approximately $(4.7 \pm 0.3)\,\%$ higher than 'normal'. For comparison, sample-to-sample variability in ion–current ratios are typically within 0.3 % of standard values.

We are still investigating the origin of this anomalous isotopic shift. The analyses of both samples were reproducible within the stated uncertainty when re-measured

Table 1 Isotopic composition of the argon gas used in the two isotherms

Argon gas	Ion current ratio $[^{36}Ar/^{40}Ar]$	Ion current ratio $[^{38}Ar/^{40}Ar]$	Molar mass[Ar] $(g \cdot mol^{-1})$
BIP+ ('fixed' exp)	0.003 357 70	0.000 661 33	39.947 706 21
BIP ('hung' exp)	0.003 333 50	0.000 633 54	39.947 857 10

The analysis indicates a difference of 3.77 parts in 10^6

Table 2 Chemical impurity analysis

	Sample 1		Sample 2	
	Upper limit	Uncertainty	Upper limit	Uncertainty
N_2	2	2	2	2
O_2	0.1	0.1	0.3	0.1
H_20	0.1	0.1	0.5	0.5
CO_2	0.5	0.5	0.5	0.5
He	1	1	1	1
Ne	1	1	1	1
Total hydrocarbon	0.5	0.5	0.5	0.5

All figures are parts in 10^6 of amount concentration. Sample 1 was from BIP+ gas used in the 'Fixed' experiment, and Sample 2 was from BIP gas from the 'Hung' experiment

4 months later. From the perspective of this experiment, we believe the IRMM measurements establish the isotopic mass with a relative uncertainty of 0.21 parts in 10^6.

The chemical impurity analysis from IRMM is shown in Table 2. Since the gas passes through a getter before reaching our sphere, we are confident that the concentrations of the non-noble gases *in our experiment* were well below the IRMM detectability limits. However, other noble gases will also pass through the getter. At NPL, we have made *uncalibrated* mass spectrometer measurements on BIP argon and failed to find any evidence for the presence of xenon, krypton or helium, but the same experiments *did* provide evidence for the presence of neon. In addition, measurements with a cold trap by one of us (LP) indicate that levels of krypton and xenon make no detectable difference to the speed of sound in argon.

It is difficult to combine our preliminary evidence to make a realistic estimate of the uncertainty in k_B due to the presence of other noble gases in argon. Using our uncalibrated mass spectrometry as a guide, we assume that our detected neon signal corresponds to the limit of detection of the IRMM mass spectrometer (1 part in 10^6). Since the molar mass of neon is one half the molar mass of argon, this would affect our k_B result by 0.5 part in 10^6. We consider that the maximum likely effect is twice this value. This is consistent with agreement between our two results of 1 part in 10^6 after correcting for different *isotopic* composition, and this agreement is itself broadly consistent with the hypothesis that levels of other noble gases are significantly lower than the mass spectroscopic detection limits.

2.6 Acoustics

The (0, 2) to (0, 10) acoustic radial modes were measured six times at each pressure using two 1/4" *GRAS* 40 BP microphones [16]. The source transducer was fitted with a transmitter adapter (*GRAS* Type RA0086) and driven from a frequency-synthesised sine wave generator (*SRS DS335*) [26] locked to a rubidium clock (*SRS SIM940*). The transducer was polarised to 130 V and driven at 60 V peak-to-peak by a *Krohn-Hite* 7602 M wide band amplifier [27]. The microphone was connected directly to a *GRAS* Type 26AC preamplifier within the pressure chamber, and then via feedthroughs to a *GRAS* Type 12AA power module and from there to a lock-in amplifier (*SRS 830*). Before each isotherm, both the sphere and pressure vessel were evacuated, and tests during that time showed that there was no detectable microphone signal. This indicates that electrical cross talk between the driver and detector transducers was negligible.

Data for a single acoustic resonance was acquired by reading the lock-in at uniform frequency intervals over a range of ± 6 times the expected half-width around the expected resonance frequency. Data were taken both while increasing and decreasing the frequency, and the two data sets were averaged. The temperature, pressure and gas flow readings corresponding to the measurement were taken at the beginning and end of the resonance sweep and also averaged. Typically data from a single resonance were acquired in approximately 1 min. A fit was made to the resonance assuming a complex Lorentzian line-shape on a linear background. Residuals of fits were generally less than 0.1 % of the peak amplitude and visually random. Once the required pressure and flow set points had been reached, *LabView* [28] software controlled the data collection process creating data files containing the preliminary fitted results and the raw data for further post processing. In between the acoustic measurements, the microwave TM11 and TM12 modes were measured to track changes in the radius of the sphere with temperature and pressure.

After acquisition and initial analysis, the data from each resonance were checked. The number of data points at the frequency extremities of each data set could be adjusted until the uncertainty on the center frequency was a minimum. This adjustment was not necessary for the lower frequency (0, 2) to (0, 5) resonances which we used to estimate of k_B. However, the density of acoustic resonances and spurious shell modes at high frequencies was such that the (0, 6) to (0, 10) resonances frequently occur close to other resonances, and their positions with respect to these resonances varies through the isotherm.

2.7 Microwave Radius Estimates

Microwave measurements were made using an *Agilent* N5230A PNA-L network analyzer locked to the same SRS rubidium clock (*SRS* SIM940) used in the acoustic measurements. Two small co-axial antennae were mounted in the sphere, such that the centre conductor of each sat flush with the inner surface. The gap around each probe was filled with epoxy to minimize acoustic perturbations. The radius of the sphere was inferred from measurements of the TM11–TM16 microwave resonances made prior

to fixing the sphere in the cryostat, and confirmed *in situ* using measurements of the TM11 and TM12 resonances.

The TM11–TM16 modes were measured *before* the insertion of the acoustic transducers. The place of the acoustic transducers was filled with a copper blank which had been machined in place at the same time that the inner surface was diamond-turned. The surface thus closely matched the surrounding quasi-spherical surface. In addition to the microwave ports, two small ports carried gas in and out of the sphere. Argon gas was flowed through the sphere and the temperature and pressure of the argon was measured and results corrected for changes in argon density. For each mode studied, a frequency sweep of 201 points was made over the width of the associated triplet and a complex resonance function was fitted to the measured S_{21} parameter.

The inference of the average radius is complex and requires several corrections to be made (Table 3). After applying a skin depth correction based on the measured half-widths (Fig. 7), we apply corrections to the observed TM1n frequencies for the perturbations due to the gas inlet and outlet ducts, and the two microwave antennae. These corrections are based on an extensive study of probe effects in quasi-spheres by Underwood et al. [29]. Using values of ε_1 and ε_2 deduced from the *splitting* of the microwave resonances, we then apply the second-order shape correction based on the study of Mehl [8]. After this correction, the average radius inferred from each of the six TM1n modes studied agreed within ± 6.3 nm (Fig. 8). This demonstrates the self-consistency of both the second-order shape correction and the probe corrections.

The blank plugs were then removed and the acoustic transducers fitted. The changes in the internal surface profile were captured using *Repliset*$^{\mathrm{TM}}$ [30] resin, and the resulting replica of the surface profile was subsequently analyzed using confocal microscopy.

Inside the cryostat, measurements could only be made on the TM11 and TM12 resonances due to losses in the microwave feedthroughs and cable. The temperature dependence of the radius was deduced at constant pressure during the warm up after each experiment. The pressure dependence of the radius was measured from 50 kPa to 600 kPa and during the two isotherms was found to be, respectively, 27 % and 20 % larger than expected using the compressibility of copper reported by May et al. [31]. (7.52×10^{-12} Pa^{-1}). However, this correction amounts to only 0.3 part in 10^6 at the highest pressure. The main contribution to our uncertainty in this measurement was the changing refractive index of the argon with pressure and our value agreed with that of May et al. [31] within the uncertainty of our measurement.

In subsequent calculations of the speed of sound, we used the following expression for the radius at a given temperature and pressure:

$$a\,(T,\,P) = a_0 \left(1 - \frac{K_P}{3} P + (T - 273.16)\,K_T\right) \tag{2}$$

where K_P is the isothermal compressibility of copper 7.52×10^{-12}Pa^{-1}, K_T is the thermal expansivity of copper measured to be 16.324×10^{-6}K^{-1} at $T = 273.16$ K, and α_0 is the radius of the sphere at $T = 273.16$ K and $P = 0$ kPa, found to be 50.258 213 mm. The uncertainty on this radius estimate derives mainly from uncertainties in the probe corrections, and, in particular, on uncertainties in the effective volume of the microphones. No change was observed in ε_1 or ε_2 as a function of pressure.

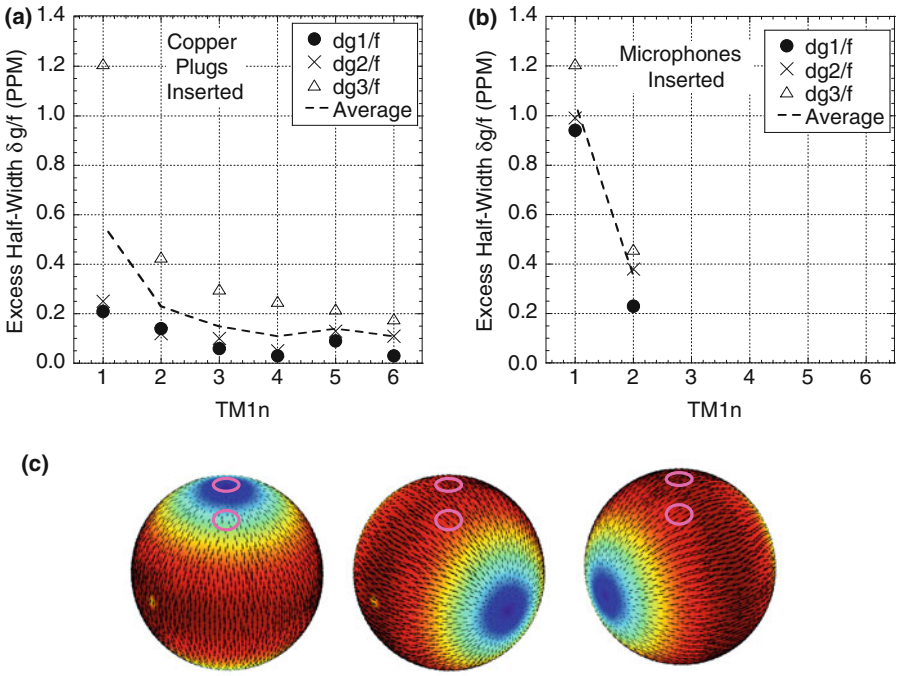

Fig. 7 Microwave excess half-widths at 20 °C. The TM11–TM16 modes measured (**a**) with the copper plugs inserted, and (**b**) with the microphones inserted. (**c**) The surface current density for the TM11 modes showing the position of microphones. The shading shows the time-averaged surface current density and the arrows show the current direction (at phase angle 0 °). The excess half-widths increase after inserting the microphones only for the modes (center and right) which have regions of high surface current density in the vicinity of the microphones

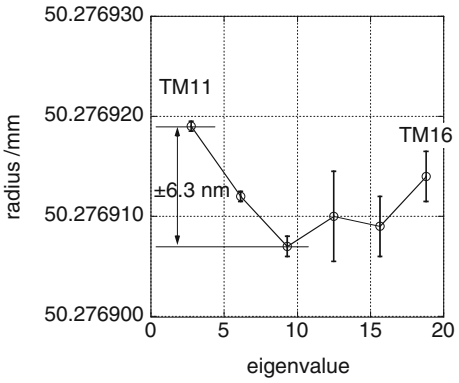

Fig. 8 Radius estimates for TCU1 from the TM11 to TM16 modes after correction for probe and second-order shape effects. The error bars show the Type A uncertainties while the scatter of the data is an indication of the self-consistency of the probe corrections. The data correspond to a temperature of 22.305 °C

Measurements of the replica microphone structure implied that we should expect to see a *decrease* in volume of the sphere of 16.2 parts in 10^6, i.e., the microphones protruded slightly into the sphere. However, the microwave measurements implied a decrease in volume of only 13.1 parts in 10^6. This difference amounts to a discrepancy of 1 part in 10^6 on the average radius, and we consider this difference to be a likely

Table 3 Second-order shape correction and corrected radii

	Fixed	Hung	
Mode	TM11	TM11	TM12
Fitted $p = 0$ radius / mm	50.258318	50.258313	50.258250
Linear fit term/ mm · kPa^{-1}	-1.60×10^{-7}	-1.51×10^{-7}	-1.53×10^{-7}
ε_1	0.001048	0.001048	0.001051
ε_2	0.000796	0.000796	0.000801
Second-order correction	0.16	0.16	0.95
Correction per duct	−1.04	−1.04	−0.87
Correction per probe	−1.04	−1.04	−0.87
Corrected $p = 0$ radius/ mm	**50.258 213**	**50.258 216**	**50.258 210**

The corrections are expressed in parts in 10^6 and refer to radii at the triple point of water
Bold value shows final radii after correction that are used in later calculations

Table 4 Summary of the measurement and post-processing procedure to obtain the Boltzmann constant

§3.1	Acquire raw data and determine centre frequencies $f(0, n)$ and half-widths $g(0, n)$
§3.2	Evaluate and apply corrections for the thermal boundary layer and bulk dissipation
§3.3	Evaluate and apply correction for ducts
§3.4	Assess excess half-widths
§3.5	Evaluate and apply correction for transducer compliance
§3.6	Evaluate and apply second-order correction for quasi-spherical distortion
§3.7	Evaluate $c^2(T, P)$ using the radius deduced from microwaves
§3.8	Correct data from measurement temperature to the temperature of the triple point of water
§3.9	Fit isotherms for each mode separately
§3.10	Evaluate and apply shell correction
§3.11	Fit isotherms for combined (0, 2) to (0, 5) data
§3.12	Further analysis of isotherms and calculation of k_B

The left-hand column shows the section number in which that part of the procedure is discussed

estimate of the Type B uncertainty in the radius estimation. This makes a contribution of 2 parts in 10^6 to our uncertainty in k_B, easily the largest contribution.

3 Analysis

A summary of the measurement and post-processing procedure used to obtain the Boltzmann constant is shown in Table 4.

3.1 Step 1: Raw Data

Figure 9 shows typical raw data for the (0, 3) radial acoustic mode measured with argon gas. The fitting uncertainty on the center frequency is 9 parts in 10^9.

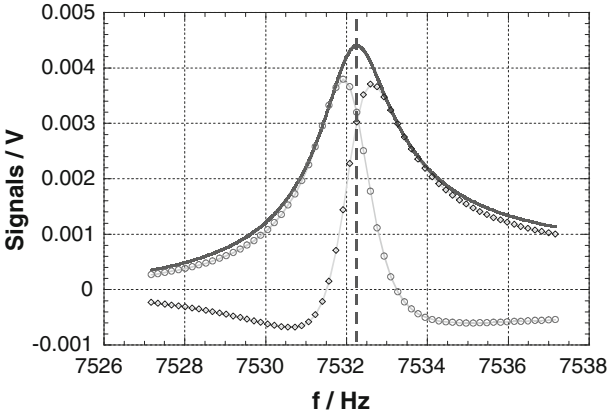

Fig. 9 Typical raw signals for the (0, 3) radial mode for argon at $P = 300$ kPa. The data points correspond to the in-phase and out-of-phase signals from the lock-in, and the *solid line* is the computed signal magnitude

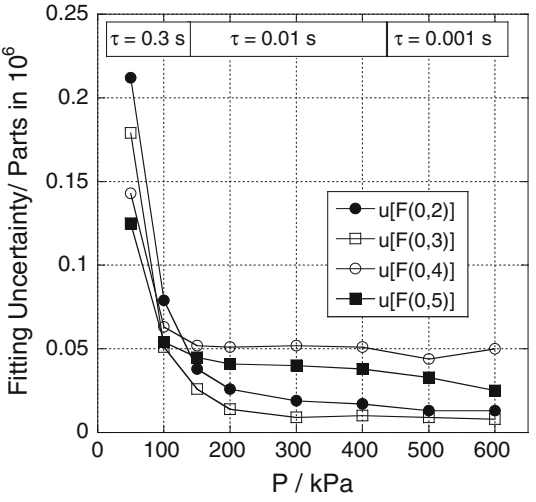

Fig. 10 Typical fitting uncertainty of the center frequency shown as a function of pressure. The lock-in time constant used at each pressure is shown at the *top* of the figure

Figure 10 shows the typical fitting uncertainty $u(k = 1)$ on the center frequency of the lowest four radial modes. The *lock-in* time constant is also shown on the figure.

3.2 Step 2: Thermal Boundary Layer and Bulk Dissipation Correction

The thermal boundary layer (TBL) is a layer of gas near the walls of the resonator in which the periodic temperature oscillations associated with the acoustic pressure oscillations are reduced because of the enhanced thermal conductivity of the walls. It forms the largest single correction to the resonant frequencies, and amounts in our case to approximately 336 parts in 10^6 for the (0, 2) resonance at 50 kPa, falling to only 51 parts in 10^6 for the (0, 6) resonance at 600 kPa. It also contributes significantly

to the broadening of the resonances. For our target uncertainty, the TBL correction must therefore be estimated with a relative uncertainty of approximately 1 part in 10^3 or better. Based on the studies by Oxborrow [12], Benedetto et al. [6] and Moldover et al. [4], the TBL correction is estimated from

$$\frac{\Delta f_{\mathrm{TBL}}}{f} = \frac{-(\gamma-1)}{2a}\delta_{\mathrm{th}} + \frac{(\gamma-1)}{a}l_{\mathrm{th}} + \frac{(\gamma-1)}{2a}\delta_{\mathrm{th,Cu}} \cdot \frac{\lambda_{\mathrm{Gas}}}{\lambda_{\mathrm{Shell}}} \tag{3}$$

$$\frac{g_{\mathrm{TBL}}}{f} = \frac{(\gamma-1)}{2a}\delta_{\mathrm{th}} + \frac{(\gamma-1)}{2a}\delta_{\mathrm{th,Cu}} \cdot \frac{\lambda_{\mathrm{Gas}}}{\lambda_{\mathrm{Shell}}} \tag{4}$$

where $\Delta f_{\mathrm{TBL}}/f$ is the fractional change in resonance frequency and g_{TBL}/f is the fractional half-width; γ is the ratio of principal heat capacities of the gas; λ_{Gas} and λ_{Shell} are the thermal conductivities of the gas and the shell, respectively; a is the average radius of the sphere; and δ_{th} is the thermal penetration length; and l_{th} is the thermal accommodation length.

The bulk dissipation correction, which accounts for losses in the gas, broadens the resonance but does not change the frequency. Here, this correction (scaled by the frequency) amounts to approximately 31 parts in 10^6 for the (0, 6) resonance at 50 kPa, falling to only 1 part in 10^6 for the (0, 2) at 600 kPa. The bulk dissipation contribution to the half-width is given by

$$\frac{\Delta g_{\mathrm{BULKDIS}}}{f} = f^2\frac{\pi^2}{u^2}\left[\frac{4}{3}\delta_{\mathrm{v}}^2 + (\gamma-1)\,\delta_{\mathrm{th}}^2\right] \tag{5}$$

where u is the speed of sound and δ_{v} is the viscous penetration length. The TBL and bulk dissipation corrections were *subtracted* from the raw data to estimate the 'ideal' resonance frequencies and half-widths.

The uncertainties in the TBL and bulk dissipation terms arise from the uncertainties in the quantities listed in Table 5. The terms include: the measured parameters T, P, M(Ar), and a; the thermophysical properties λ_{Gas}, η_{Gas} (viscosity); 2nd and 3rd virial coefficients; and the derivatives of the 2nd and 3rd virial coefficients with respect to T. We have estimated the uncertainty in Eqs. 3 to 5 using the uncertainty in each parameter shown in Table 5.

We calculate the combined uncertainty due to the TBL and bulk dissipation correction by quadrature summation. Figure 11 shows the uncertainty for the frequency and half-width for the (0, 2) to (0, 6) radial modes.

Over the pressure range 50 kPa to 600 kPa, the uncertainties vary from 0.26 part in 10^6 to 0.1 part in 10^6 for $\Delta f/f$ moving from the (0, 2) to (0, 10) mode, and from 0.28 part in 10^6 to 0.17 part in 10^6 for g/f moving from the (0, 2) to (0, 10) mode. At the highest measurement pressure of 600 kPa, the uncertainties in $\Delta f/f$ and g/f are less than 0.1 parts in 10^6 for all modes.

Table 5 Input parameter uncertainties used to determine the uncertainty in the TBL and bulk dissipation correction

Parameter	Description	Parameter standard uncertainty
T	Temperature	50 mK
P	Pressure	10 Pa
M(Ar)	Molar mass	0.1 %
a	Radius	0.1 %
λ	Thermal conductivity	0.1 %
η	Viscosity	0.1 %
B	2nd virial coefficient	1.0 %
$\mathrm{d}B/\mathrm{d}T$	1st derivative of 2nd virial coefficient w.r.t T	1.0 %
$\mathrm{d}^2B/\mathrm{d}T^2$	2nd derivative of 2nd virial coefficient w.r.t. T	1.0 %
C	3rd virial coefficient	10.0 %
$\mathrm{d}C/\mathrm{d}T$	1st derivative of 3rd virial coefficient w.r.t T	10.0 %
$\mathrm{d}^2C/\mathrm{d}T^2$	2nd derivative of 3rd virial coefficient w.r.t. T	10.0 %

All parameter estimates refer to the triple point of water

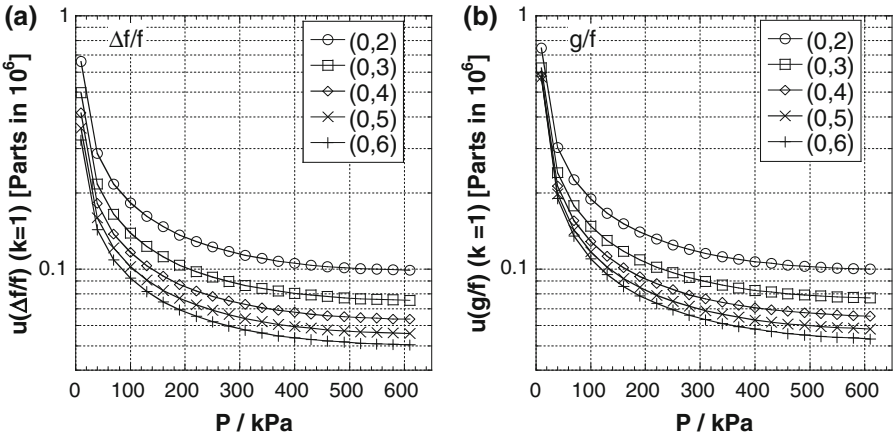

Fig. 11 Combined standard uncertainty in the TBL and bulk dissipation correction for (**a**) the frequency $\mathrm{u}(\Delta f/f)$ and (**b**) the half-width $\mathrm{u}(g/f)$. The vertical scale is logarithmic

3.3 Step 3: Duct Correction

The tubes—referred to acoustically as *ducts*—carrying gas into and out of the sphere affect the experiment in several ways. Firstly, to the extent that acoustic energy is reflected from the end of the tube, the resonance frequency is shifted. Secondly, to the extent that energy is dissipated in the tube, the half-width of the sphere resonance is perturbed. Finally, to the extent that the tube represents a flow impedance, the pressure measured outside the sphere does not reflect the pressure inside the sphere.

The first two perturbations are dealt with by modelling based on the study of Mehl et al. [7]. The inlet tube is 6 m long, and almost no acoustic energy is reflected back into the sphere. Instead, the tube increases the half-width of the resonances. The outlet tube is more problematic. This is made short to minimize the pressure difference between the inside and the outside of the sphere. Our measurements indicate the pressure difference is given by

$$\Delta P = c\frac{Q}{P} \quad \text{where} \quad c = 307 \times 10^3 \ \frac{\text{Pa}^2}{\text{SCCM}} \tag{6}$$

where Q is the flow rate and P is the pressure. This correction was largest for the 'fixed' isotherm when the largest flow rate of 50 SCCM was used. At the lowest pressure 50 kPa, the pressure correction is 307 Pa. For the 'hung' isotherm, the largest correction was 10 times smaller due to the lower flow rate.

The method of equivalent T circuits [5] was used to determine the acoustic impedance of each duct and consequently the perturbation to the resonance frequencies and half-widths. The inlet duct consisted of two cylindrical ducts in series. The first, attached to the sphere, had a length of $L_1 = 100$ mm and a radius $r_1 = 0.254$ mm. The second, attached to the first, had a length of $L_2 = 6000$ mm and a radius of $r_2 = 0.572$ mm. This second duct was coiled around the middle of the outside of the sphere and then connected to the feed-in pipe work of the pressure vessel. The outlet duct consisted of a single tube of length $L = 50$ mm and radius $r = 0.381$ mm which vented directly into the pressure vessel.

Figures 12 and 13 show the results of a calculation of the combined inlet and outlet duct perturbations in $\Delta f/f$ and g/f, respectively. The $(0, 2)$ mode shows the largest variation with pressure. These perturbations were *subtracted* from the measured values of $f(0, n)$ and $g(0, n)$. An analysis of the sensitivity of the duct correction to the radii of the ducts closest to the sphere indicates that a 5 % uncertainty in the radii can result in a change of up to 0.1 parts in 10^6 on the frequency correction.

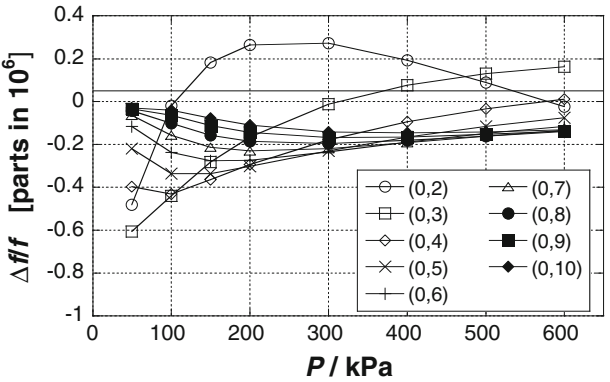

Fig. 12 Combined inlet and outlet duct frequency perturbation

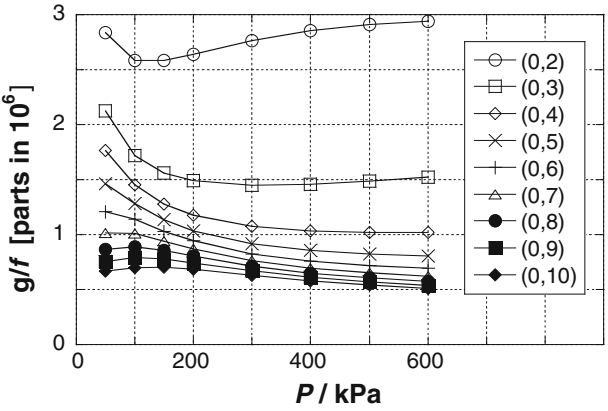

Fig. 13 Combined inlet and outlet duct half-width perturbation

3.4 Step 4: Assess Excess Half-Widths

The 'excess' half-width Δg is the width of the resonance which is unaccounted for by the effects discussed in §3.2 and §3.3 The assessment of the excess half-width is important because it is one measure of the magnitude of unexplained or unanticipated physics, and gives an order-of-magnitude estimate for any possible *frequency* shifts which might affect the inference of k_B.

Figures 14 and 15 show the excess half-widths for the 'fixed' and 'hung' isotherms, respectively. The excess half-widths are small for the first four modes, grow larger around the (0, 6) mode, and fall for the remaining higher-order modes. The strong peak in the excess half-width is due to the interaction between the radial acoustic modes and the breathing mode of the shell.

The excess half-width versus pressure for the lowest four modes is shown in detail in Fig. 16. The data are similar for the two isotherms. The 'excess' half-width is negative for the (0,2) mode but varies linearly with pressure for the (0, 3) to (0, 5) modes, and extrapolates to zero within 0.5 parts in 10^6. This indicates that the data have been 'over-corrected' or that there is some 'mode narrowing' process occurring. Despite extensive investigation, the origin of this negative 'excess' half-width has not become apparent. Taking account of the weak statistical weighting of the low pressure points, we have assigned a conservative uncertainty of 0.7 parts in 10^6 in the resonant frequencies (shown as a dotted line in Fig. 16) to account for the unknown physics behind this effect. This leads to an uncertainty of 1.4 parts in 10^6 in our estimate of k_B.

3.5 Step 5: Transducer Compliance Correction

Based on the study of [4], the frequency shifts to the radial modes induced by the presence of two condenser microphones can be calculated using:

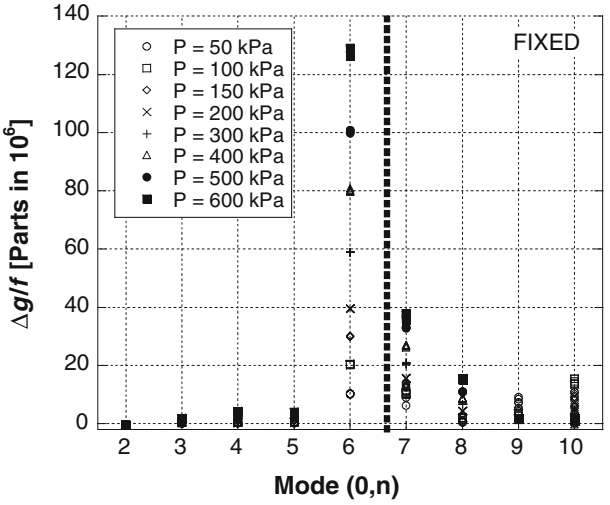

Fig. 14 Excess half-width for the 'fixed' isotherm. The *dotted line* shows the approximate location of the breathing mode as deduced in §3.10

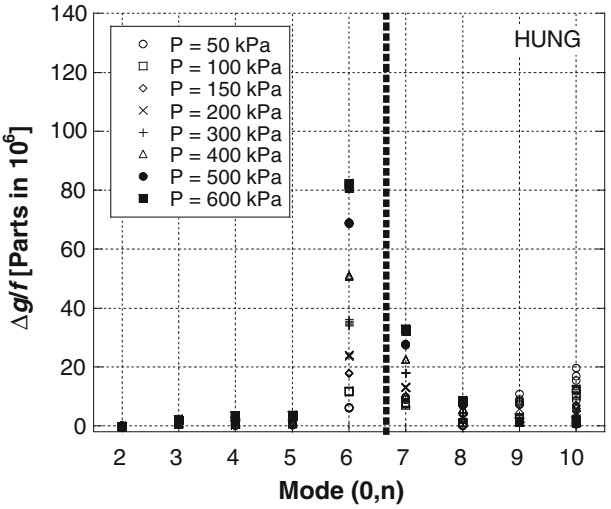

Fig. 15 Excess half-width for the 'hung' isotherm. The *dotted line* shows the approximate location of the breathing mode as deduced in §3.10

$$\frac{\Delta f_{\mathrm{tr}}}{f_{0\mathrm{n}}} = -\frac{\rho c^2 X_{\mathrm{m}} r_{\mathrm{tr}}^2}{2a^3} \tag{7}$$

where ρ is the gas density, X_{m} is the compliance per unit area of the microphone ($1.5 \times 10^{-10}\,\mathrm{m \cdot Pa^{-1}}$) and r_{tr} is the radius of the microphone. Figure 17 shows the fractional frequency perturbation *subtracted* from the measured values of

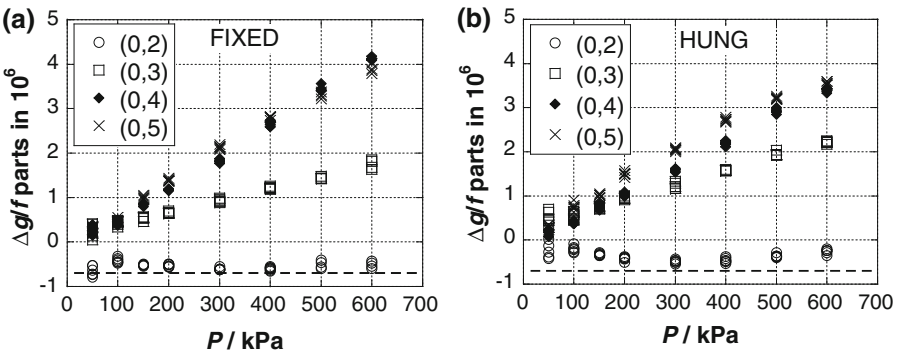

Fig. 16 Excess half-width for lower order modes for (**a**) 'Fixed' and (**b**) 'Hung' isotherms. The *dotted line* indicates the maximum negative 'excess' half-width of the (0, 2) resonance of approximately 0.7 parts in 10^6

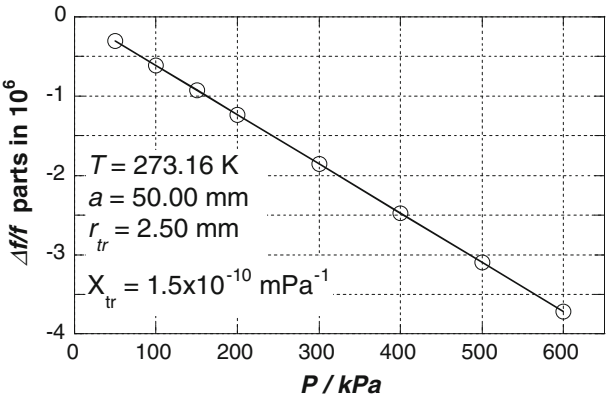

Fig. 17 Transducer perturbation to the resonant frequency

$f(0, n)$. Accounting for the two microphones, this perturbation can be expressed as $\frac{1}{P}\frac{\Delta f}{f} = -0.00619$ parts in 10^6 kPa^{-1}.

Guianvarc'h et al. [32] have proposed a more complex model for the transducer perturbation in which, compared to Fig. 17, the frequency shift differs with mode number. Since the perturbation for the lowest four radial modes (0,2) to (0,5) (used in the determination of k_B in this study) are still approximately linear in pressure and of similar magnitude, this more sophisticated model has not been applied to the data. However, this will not affect the zero pressure intercept of our isotherms.

3.6 Step 6: Second-Order Shape Perturbation

The second-order shape perturbation to the acoustic modes accounts for the fact that the resonator is a triaxial ellipsoid rather a sphere. It is evaluated based on the method of Mehl [9] and calculated using:

Table 6 Second-order shape perturbation to radial acoustic modes calculated for a triaxial ellipsoid with $\varepsilon_1 = 0.001051$ $\varepsilon_2 = 0.000801$ deduced from microwave measurements

Mode	$z(0, n)$	$\Delta f/f$ (parts in 10^6)
2	4.493 409 458	0.539
3	7.725 251 836	1.593
4	10.904 121 659	3.174
5	14.066 193 912	5.282
6	17.220 755 272	7.917
7	20.371 302 959	11.079
8	23.519 452 498	14.768
9	26.666 054 259	18.984
10	29.811 598 790	23.727

$$\frac{\Delta z_n^2}{z_n^2} = \frac{8 z_n^2}{135}\left(\varepsilon_1^2 - \varepsilon_1\varepsilon_2 + \varepsilon_2^2\right) \tag{8}$$

where z_n is the eigenvalue of the nth radial mode and ε_1 and ε_2 are the eccentricities of the sphere calculated from microwave measurements (Table 3). In order to correct the frequency (not c^2), we divide this perturbation by two and subtract it from the measurements. Table 6 shows the second-order shape perturbation.

3.7 Step 7: Calculation of the Speed of Sound Squared

The frequency measurements are converted to the speed of sound squared, c^2, using

$$c^2 = \left(\frac{2\pi f_n}{z_n}\right)^2 a^2(T, P) \tag{9}$$

where f_n is the frequency of the nth mode and z_n the corresponding eigenvalue. The radius of the sphere at the measurement temperature and pressure T and P, $a(T, P)$ is given by Eq. 2.

3.8 Step 8: Correction of Resonance Frequencies to $T = 273.16\,\mathrm{K}$

The resonance frequencies were corrected to the equivalent frequency at the triple point of water, T_{TPW} (273.16 K), using

$$f_n\left(T_{\mathrm{TPW}}, P\right) = f_n\left(T_{\mathrm{meas}}, P\right) \cdot \left(\frac{T_{\mathrm{TPW}}}{T_{\mathrm{meas}}}\right)^{1/2} \frac{\left(1 + \frac{\beta(T_{\mathrm{TPW}})}{RT_{\mathrm{TPW}}} P\right)^{1/2}}{\left(1 + \frac{\beta(T_{\mathrm{meas}})}{RT_{\mathrm{meas}}} P\right)^{1/2}} \tag{10}$$

Uncertainty in this correction arises from uncertainty in the temperature of the gas within the sphere, which is inferred from measurements of the sphere temperature via

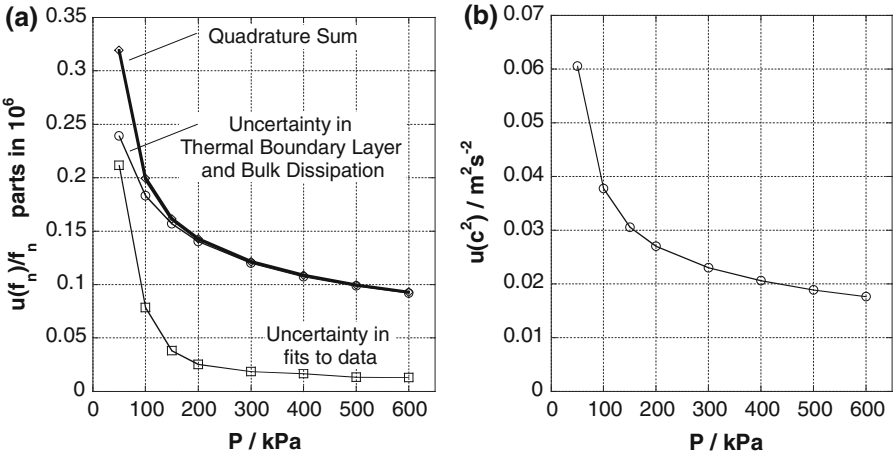

Fig. 18 (**a**) Fractional uncertainty of resonance frequency taking into account the fitting uncertainty and the uncertainty in the TBL and bulk dissipation correction. (**b**) Combined uncertainty on c^2 versus pressure

the cSPRTs. We estimate the uncertainty in the gas temperature, assuming the temperature at the equator of the sphere is representative, to be of the order $\Delta T = 0.25$ mK and convert this uncertainty in T to uncertainty in f by

$$\frac{\Delta f_n}{f_n} \approx \frac{1}{2}\frac{\Delta T}{T_{\mathrm{TPW}}} \tag{11}$$

which gives a fractional uncertainty of 0.46 parts in 10^6 in our estimation of the frequency of resonances at T_{TPW}. Since k_{B} is related to the speed of sound *squared*, this translates into an uncertainty of 0.92 parts in 10^6 in k_{B}.

3.9 Step 9: Mode-by-Mode Isotherm Analysis

In order to make a meaningful fit of the c^2 versus pressure data, the uncertainty of each c^2 datum was evaluated. Summing the uncertainty on the fitted resonance frequencies (Fig. 10) and those due to the TBL and bulk dissipation corrections (Fig. 11) in quadrature, we calculated the combined uncertainty on f_n (Fig. 18a). Re-casting in absolute c^2 units, the uncertainty varies from $0.018\,\mathrm{m}^2\cdot\mathrm{s}^{-2}$ at 600 kPa to $0.061\,\mathrm{m}^2\cdot\mathrm{s}^{-2}$ at 50 kPa. (Fig 18b). The c^2 versus P data for each individual mode was then fitted to

$$c^2 - A_3P^3 = A_0 + A_1P + A_2P^2 + A_{-1}P^{-1} \tag{12}$$

where $A_3 = 1.45\times10^{-9}\mathrm{m}^2\cdot\mathrm{s}^{-2}\cdot\mathrm{kPa}^{-3}$ [4] the P^{-1} term allows for any imprecision in the thermal accommodation coefficient (h) to be fitted.

Figure 19 shows the fitted parameters (A_0, A_1, A_2, A_{-1}) determined with a weighted least squares fit (using the uncertainty given in Fig. 18). We see that the first four modes (0, 2) to (0, 5) yield reasonably consistent values of the parameters,

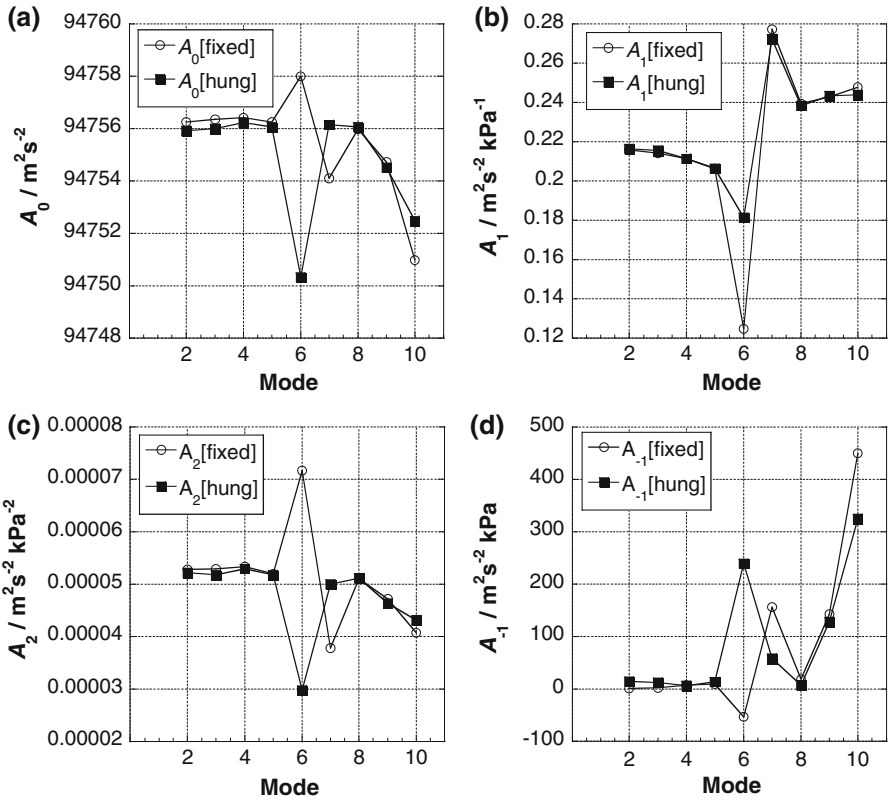

Fig. 19 Fit parameters for each mode using Eq. 13: (**a**) A_0, (**b**) A_1, (**c**) A_2, (**d**) A_{-1}

but the higher order modes do not. The (0, 6) and (0, 7) modes are significantly affected by interactions with the shell's breathing mode resonance whereas the centre frequency of higher order modes (0, 9) and (0, 10) were not fitted well due to modal overlap at high frequencies. For this reason, only the (0, 2) to (0, 5) data were included in further processing. The (0, 8) data initially looked relatively unperturbed but later tests showed that it was positioned in a modally complex region of the vibrational spectrum.

The fitting residuals are shown in Fig. 20a–h.

3.10 Assessment of the Shell Breathing Mode Correction

Using the first four radial modes (0, 2) to (0, 5) as candidates for determination of the Boltzmann constant, the perturbation to the c^2 data due to the breathing mode was estimated. Based on the procedure of Pitre et al. [5], we determined the shell correction for each mode *and* the second acoustic virial coefficient. We assume that the shell perturbation reduces c^2 by $\Delta\, c^2_{\text{shell}}$ given by

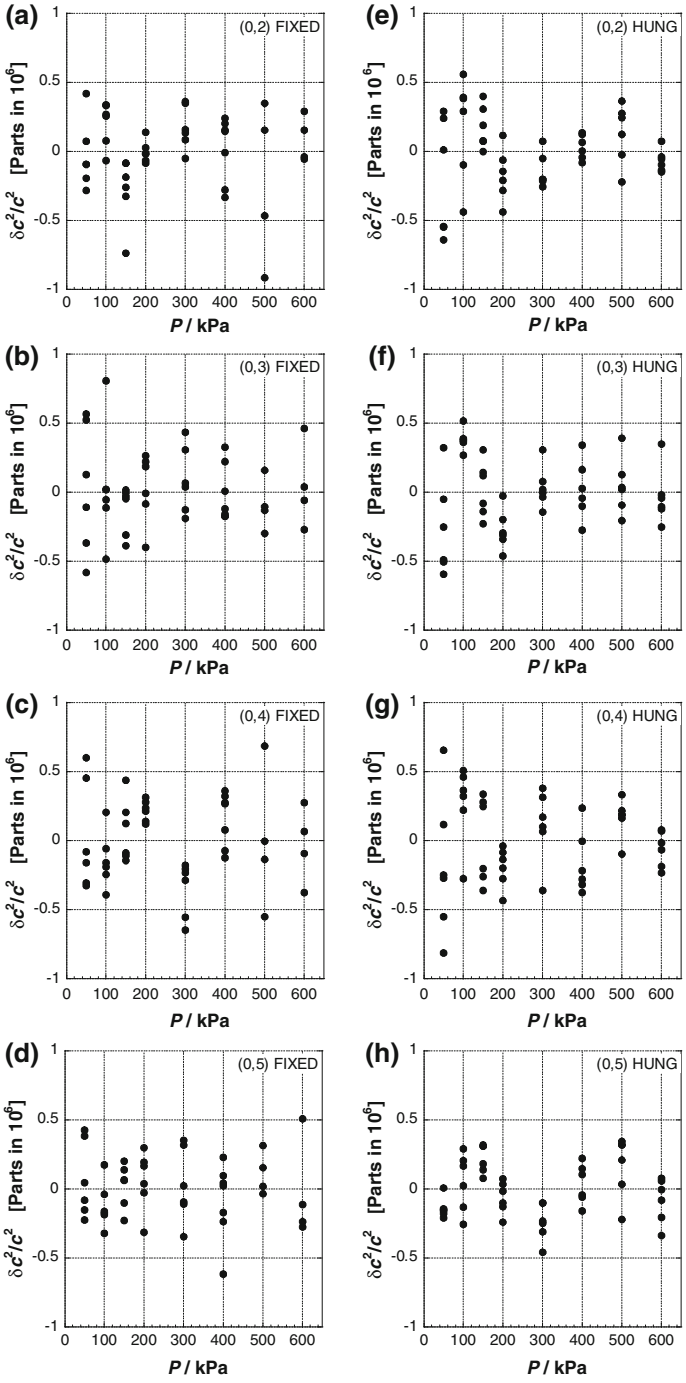

Fig. 20 (**a**–**d**) Residuals for the (0, 2) to (0, 5) modes for the 'fixed' c^2 versus P isotherm. (**e**–**h**) Residuals for the (0, 2) to (0, 5) modes for the 'hung' c^2 versus P isotherm

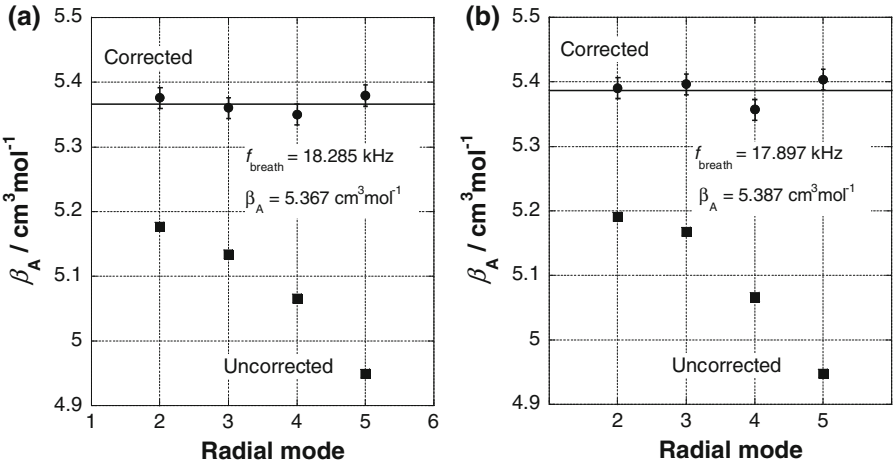

Fig. 21 Determination of the breathing mode frequency for TCU1 by removing the mode dependence of the second acoustic virial coefficient β_A. (**a**) 'Fixed' isotherm (**b**) 'Hung' isotherm

$$\frac{\Delta\, c^2_{\text{shell}}}{c^2} \approx \frac{2\kappa P}{1-\left(f_{(0,n)}/f_{\text{breath}}\right)^2} \tag{13}$$

where P is the pressure; $f_{(0,n)}$ is the nominal frequency of the nth radial acoustic mode; $f_{\text{breath}}$is the frequency of the shell breathing mode; and κ is given by

$$\kappa = \frac{5a}{\rho_{\text{shell}} u^2_{\text{shell}}} \tag{14}$$

where a is the sphere's inner radius, t is the shell thickness, ρ_{shell} is the density of the shell, and u^2_{shell} is the longitudinal speed of sound in the shell material (copper). The c^2 data versus pressure for each isotherm was fitted using

$$c^2 - A'_3 P'^3 = A_0 + A'_1 P' + A'_2 P'^2 + A'_{-1} P'^{-1} \tag{15}$$

where P' is the pressure in kPa. Based on the study of [5], we divide both sides of Eq. 18 by A_0 and re-cast it in SI pressure units leading to

$$\frac{c^2}{A_0} - \frac{A_3 P^3}{A_0} = 1 + A_1 P + A_2 P^2 + A_{-1} P^{-1} \tag{16}$$

with Eq. 16 in this form, the *second acoustic virial coefficient* is given by

$$\beta_A = RT A_1 \tag{17}$$

Table 7 Parameter values used for estimating the shell breathing mode frequency

Parameter	Value	Parameter	Value
a_0 (mm)	50.258213	K (Pa^{-1})	4.1421×10^{-11}
t (m)	0.005	a_0 ($m^2 \cdot s^{-2}$)	94756.4826
ρ_{Cu} ($kg \cdot m^{-3}$)	8933	R ($J \cdot mol^{-1} \cdot K^{-1}$)	8.314472
u_{Cu} ($m \cdot s^{-1}$)	4757.9	T (K)	273.16

Table 8 Fit parameters and correction term (*) for shell perturbation: TCU1—'Fixed' isotherm

Radial mode	f_n (Hz)	A'_1 ($m^2 \cdot s^{-2} \cdot kPa^{-1}$)	A_1 (Pa^{-1})	β_A ($cm^3 \cdot mol^{-1}$)	β_A(corr) ($cm^3 \cdot mol^{-1}$)	$1/P^* \Delta c^2/c^2$(*)
2	4380.71435	0.21598	2.2793×10^{-9}	5.1767	5.3763	8.78869×10^{-11}
3	7531.50183	0.21420	2.2606×10^{-9}	5.1342	5.3608	9.97694×10^{-11}
4	10630.6453	0.21136	2.2305×10^{-9}	5.0659	5.3501	1.25144×10^{-10}
5	13713.4125	0.20651	2.1794×10^{-9}	4.9498	5.3798	1.89351×10^{-10}

$f_{breath} = 18.285$ kHz and $\beta_A = 5.367\ cm^3 \cdot mol^{-1}$. The data for β_A and β_A(corr) are plotted in Fig. 21

As a consequence of Eq. 13, A_1 shows a frequency-dependent correction given by

$$\frac{2\kappa}{1 - \left(f_{(0,n)}/f_{breath}\right)^2} \tag{18}$$

Since physically we expect the virial coefficient to be frequency independent, the procedure for determining the shell correction involves adjustment of f_{breath} in Eq. 18 until the apparent frequency dependence of β_A is removed. Figure 21 shows the result for both isotherms. The estimated breathing mode frequencies are 18.285 kHz for the 'fixed' isotherm and 17.897 kHz for the 'hung' isotherm. The values for β_A are $5.367\ cm^3 \cdot mol^{-1}$ and $5.387\ cm^3 \cdot mol^{-1}$ for the 'fixed' and 'hung' isotherms, respectively. These values are respectively 0.90 % and 0.53 % lower than the value found by Pitre et al. [5]. Table 7 shows the values of the parameters used in the model.

Tables 8 and 9 show the fit parameters and the correction term that was added to the c^2 data to account for the shell perturbation for the 'Fixed' and 'Hung' experiments respectively. Once these corrections have been made, the c^2 versus P isotherms for the (0, 2) to (0, 5) data can be directly compared, and fitted with a single curve.

3.11 Isotherm Analysis of Combined (0, 2) to (0, 5) Mode Data: Determination of A_0

With the breathing mode shell correction applied to the (0, 2) to (0, 5) mode data, a single fit (Eq. 13) was applied to the combined data set (Fig. 22).

Although the data is fitted with a single curve, the residuals for each mode can be identified by their grouping (Fig. 22b, d). This implies that there is an as yet unidentified systematic mode-dependent effect. In order to investigate the implications of

Table 9 Fit parameters and correction term (*) for shell perturbation: TCU1—'Hung' isotherm

Radial mode	f_n (Hz)	A'_1 ($m^2 \cdot s^{-2} \cdot kPa^{-1}$)	A_1 (Pa^{-1})	β_A ($cm^3 \cdot mol^{-1}$)	β_A(corr) ($cm^3 \cdot mol^{-1}$)	$1/P^* \Delta c^2/c^2$ (*)
2	4380.714347	0.21656	2.2855×10^{-9}	5.1908	5.3909	8.81220×10^{-11}
3	7531.501834	0.21562	2.2755×10^{-9}	5.1681	5.3967	1.00671×10^{-10}
4	10630.64532	0.21139	2.2309×10^{-9}	5.0667	5.3574	1.28007×10^{-10}
5	13713.41252	0.20645	2.1787×10^{-9}	4.9483	5.4040	2.00653×10^{-10}

$f_{\text{breath}} = 17.897$ kHz and $\beta_A = 5.387\,cm^3 \cdot mol^{-1}$. The data for β_A and β_A(corr) are plotted in Fig. 21

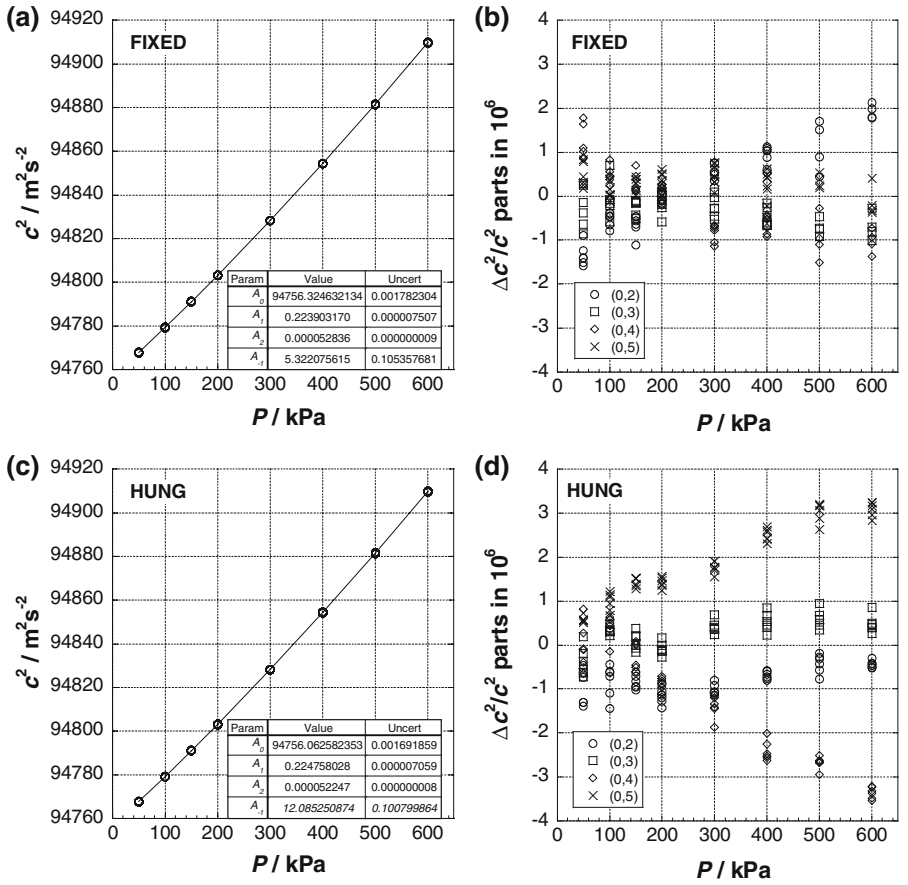

Fig. 22 Fit to the combined (0, 2) to (0, 5) modes after application of the shell correction. (**a**, **b**) show the fit and residuals for the 'fixed' isotherm and (**c**, **d**) show the fit and residuals for the 'hung' isotherm

this effect for our determination of k_B, we compared the extrapolated value of c^2 at zero pressure (A_0) determined for (a) individually fitted *non-shell corrected* (0, 2) to (0, 5) data (Fig. 20) and (b) the combined (0, 2) to (0, 5) *shell corrected* data (Fig. 22). The comparison (Table 10) indicates that independent of the way in which the shell is accounted for, the estimated value of $A_0(c^2)$ is the same to less than 0.04 parts in 10^6. The analysis indicates that A_0 for the 'hung' isotherm is 2.77 parts in 10^6 lower than that of the 'fixed' isotherm.

The Boltzmann constant is deduced from the acoustic data using

$$k_B = \frac{M(\mathrm{Ar})\, c_0^2}{\gamma_0 N_A T_{TPW}} \tag{19}$$

where $M(\mathrm{Ar})$ is the mean molar mass of the gas, N_A is the Avogadro number, c_0 is the speed of sound at $T = 273.16\,\mathrm{K}$ in the limit of zero pressure, and γ_0 is the zero pressure limit of the ratio of molar heat capacities. Using the value for c^2 given in Table 10, we can estimate the Boltzmann constant from the two isotherms. Table 11 summarizes our preliminary estimate of k_B.

Table 11 shows that the difference of 2.77 parts in 10^6 between our two estimates of the zero pressure limit of c^2, is in large part due to the change in the isotopic composition of the argon used. The difference between the inferred values of k_B between the 'fixed' and 'hung' isotherms is 1.01 parts in 10^6.

3.12 Further Analysis of Isotherms

We carried out extensive investigations of alternative fitting procedures for analyzing the two isotherms, including different techniques of accounting for the P^3 and P^{-1} terms. Six different analysis procedures were considered and the data re-fitted for each procedure (Table 12). We tested the effect of varying the A_3 coefficient and subtracting the $A_3 P^3$ from the c^2 data before fitting the remaining parameters; or fitting this parameter. In addition, we tested the effect of fixing and subtracting the value of the A_{-1} term by using either individually fitted, or average, values of h, the thermal accommodation coefficient. The six procedures are summarized in Eq. 20 in which parameters to the left of the equality are fixed and parameters to the right are fitted to the data.

$$\begin{array}{lll}
c^2 - A_3 P^3 & = A_0 + A_1 P + A_2 P^2 + A_{-1} P^{-1} & [1, 2]\ A_3 \text{ fixed \& } A_{-1} \text{ fitted} \\
c^2 & = A_0 + A_1 P + A_2 P^2 + A_3 P^3 + A_{-1} P^{-1} & [3]\ A_3 \text{ \& } A_{-1} \text{ terms fitted} \\
c^2 - A_{-1} P^{-1} & = A_0 + A_1 P + A_2 P^2 + A_3 P^3 & [4]\ A_3 \text{ fitted \& } h \text{ fixed at average value} \\
c^2 - A_3 P^3 - A_{-1} P^{-1} & = A_0 + A_1 P + A_2 P^2 & [5]\ A_3 \text{ \& } h \text{ fixed at average value} \\
c^2 - A_3 P^3 - A_{-1} P^{-1} & = A_0 + A_1 P + A_2 P^2 & [6]\ A_3 \text{ \& } h \text{ fixed for each isotherm}
\end{array} \tag{20}$$

For the initial estimate of k_B (Table 11) we set $A_3 = 1.45 \times 10^{-9}\,\mathrm{m^2 \cdot s^{-2} \cdot kPa^{-3}}$ as used by Moldover et al. [4] on the basis of a study done by Goodwin [37]. This is given as Fit 1 in Table 12. This predicts k_B values 1.181 parts in 10^6 and 0.175 parts

Table 10 The zero pressure speed of sound squared for TCU1 for 'fixed' and 'hung' isotherms

Analysis	Radial Mode Index	Fixed		Hung		
		$A_0\,(\mathrm{m}^2\cdot\mathrm{s}^{-2})$	$u(A_0)\,(\mathrm{m}^2\cdot\mathrm{s}^{-2})$	$A_0\,(\mathrm{m}^2\cdot\mathrm{s}^{-2})$	$u(A_0)\,(\mathrm{m}^2\cdot\mathrm{s}^{-2})$	Difference (parts in 10^6)
Individual fitting of each *non-shell corrected* mode	2	94756.2498	0.0074	94755.9189	0.007	−3.492
	3	94756.364	0.0074	94756.0095	0.007	−3.741
	4	94756.4214	0.0074	94756.2415	0.007	−1.898
	5	94756.2512	0.0074	94756.066	0.007	−1.955
	Aver (2–5)	**94756.3216**		**94756.0590**		**− 2.771**
Fitting of combined 2–5 shell-corrected modes	2–5	**94756.3246**	0.0018	**94756.0626**	0.0017	**−2.766**

The table shows the difference between the two analyses discussed in the text in which the four modes examined are either fitted together or separately. The analyses produce estimates for the zero pressure speed of sound squared which differ by only $0.0036\,\mathrm{m}^2\cdot\mathrm{s}^{-2}$ or 38 parts in 10^9

Bold value distinguishes average values from individual values

Table 11 The determination of the Boltzmann Constant from 'fixed' and 'hung' isotherms

Parameter	Units	Fixed	Hung	Difference (parts in 10^6)
M(Ar)	$\mathrm{kg \cdot mol^{-1}}$	0.039947706	0.039947857	**3.78**
c^2(273.16 K, 0 Pa)	$\mathrm{m^2 \cdot s^{-2}}$	94756.3246	94756.0626	**−2.77**
k_B	$\mathrm{J \cdot K^{-1}}$	$1.3806488 \times 10^{-23}$	$1.3806502 \times 10^{-23}$	1.01

Table 12 Results of six different fitting procedures on the 'fixed' and 'hung' isotherms

Fit	Description	Δk_B [fixed]—CODATA	Δk_B [hung]—CODATA	Difference	Average
[1]	Thermal accommodation fitted $h = 0.93$ Fixed Thermal accommodation fitted $h = 0.83$ Hung Fixed $A_3 = 1.45 \times 10^{-9}\ \mathrm{m^2 \cdot s^{-2} \cdot kPa^{-3}}$	−1.181	−0.175	1.006	−0.678
[2]	Thermal accommodation fitted $h = 0.93$ Fixed Thermal accommodation fitted $h = 0.84$ Hung Fixed $A_3 = 1.20 \times 10^{-9}\ \mathrm{m^2 \cdot s^{-2} \cdot kPa^{-3}}$	−1.023	−0.011	1.012	−0.517
[3]	Thermal accommodation fitted $h = 0.89$ Fixed Thermal accommodation fitted $h = 0.97$ Hung Fitted $A_3 = 2.404 \times 10^{-9}\ \mathrm{m^2 \cdot s^{-2} \cdot kPa^{-3}}$ (Fixed) Fitted $A_3 = -3.033 \times 10^{-9}\ \mathrm{m^2 \cdot s^{-2} \cdot kPa^{-3}}$ (Hung)	−1.784	2.767	4.550	0.492
[4]	Thermal accommodation corrected for $h_{aver} = 0.88$: $A_{-1} = 0$ Fitted $A_3 = 2.5935 \times 10^{-9}\ \mathrm{m^2 \cdot s^{-2} \cdot kPa^{-3}}$ (Fixed) Fitted $A_3 = -1.2480 \times 10^{-9}\ \mathrm{m^2 \cdot s^{-2} \cdot kPa^{-3}}$ (Hung)	−1.914	1.277	3.191	−0.319
[5]	Thermal accommodation corrected for $h_{aver} = 0.88$: $A_{-1} = 0$ Fixed $A_3 = 1.45 \times 10^{-9}\ \mathrm{m^2 \cdot s^{-2} \cdot kPa^{-3}}$	−1.606	0.521	2.127	−0.543
[6]	Thermal accommodation corrected for $h = 0.93$ Fixed, $h = 0.83$ Hung: $A_{-1} = 0$ Fixed $A_3 = 1.45 \times 10^{-9}\ \mathrm{m^2 \cdot s^{-2} \cdot kPa^{-3}}$	**−1.028**	**−0.124**	**0.894**	**−0.576**

The difference in k_B from CODATA 2006 value for each fitting configuration, the difference between the two isotherms, and the average value of the two isotherms. Notice the unphysical values of A_3 resulting from Fits 3 and 4, and the agreement for k_B between all the other procedures: the four estimates are covered by a range of 0.16 parts in 10^6

Bold value shows our best selected fitting procedure

in 10^6 below the CODATA 2006 value which is used as a convenient reference. Fit 2 used $A_3 = 1.20 \times 10\,\mathrm{m^2 \cdot s^{-2} \cdot kPa^{-3}}$ as recommended by Moldover et al. [4]. The change in estimated values of A_3 makes a difference of only 0.16 parts in 10^6 in our estimate of k_B

In Fits 3 and 4 we allowed the A_3 term be fitted freely. This was done while allowing the A_{-1} term to be either fitted (Fit 3) or fixed at the average value (Fit 4). Both fits gave estimates for A_3 that are physically implausible, and produced a wide dispersion in $c^2(P = 0)$ values. We do not consider these fits satisfactory.

In Fits 5 and 6 we fix the A_3 term at the value used in Fit 1, and correct for the A_{-1} term. This was done using the both the average value of the fitted A_{-1} term (Fit 5) and the individually fitted values (Fit 6). Using the individually fitted values gives estimates for k_B which are closer together (0.894 parts in 10^6 rather than 2.127 parts in 10^6) but changes the average value by only 0.033 parts in 10^6).

It might seem overly lax to allow the A_{-1} term to differ between the two isotherms, because the expected physical mechanism behind the P^{-1} term involves the accommodation coefficient, h, which would not be expected to differ between the two isotherms carried out with the same gas and the resonator. However, it is possible that there are other physical processes which also contribute to a P^{-1} behavior. Most significant in this respect is the large difference in flow rate between the two experiments (§2.4). The fixed experiment used a flow rate of 50 SCCM while the hung experiment used a flow rate of 5 SCCM. Although the physics which underlies a flow-dependent term is not clear, flow-dependent effects have been reported. [36]

On the basis that the two isotherms agree most closely, we believe that Fit 6 gives the best estimate of k_B. However, it should be noted that with the exception of Fits 3 and 4 which yield unphysical values of the third virial coefficient, the four analyses described in Table 12 yield estimates of k_B which are covered by a total span of 0.16 parts in 10^6. This gives us confidence in the robustness of our estimate and the conservative nature of our uncertainty analysis. Table 13 outlines our uncertainty budget.

We thus find

'Fixed' $k_B = 1.380\,648\,9 \times 10^{-23}\,\mathrm{J \cdot K^{-1}}$

'Hung' $k_B = 1.380\,650\,2 \times 10^{-23}\,\mathrm{J \cdot K^{-1}}$

'Average' $k_B = (1.380\,649\,6 \pm 0.000\,00\,43) \times 10^{-23}\,\mathrm{J \cdot K^{-1}}$

This average value is 0.58 parts in 10^6 below the CODATA 2006 value with the values consistent within combined ($k = 1$) uncertainties.

4 Towards a Final Measurement: Scope for Improvements

4.1 Discussion

The experiments described above were undertaken to identify limiting uncertainties, which must be overcome to determine the Boltzmann constant with an uncertainty of less than 1 part in 10^6. Some of our experimental choices were, in retrospect, sub-optimal, and we believe there is significant scope for improvement.

4.2 Shape

Recent studies [8,9] have highlighted the importance of using resonators with a shape that conforms closely to a shape amenable to modelling, ideally a triaxial ellipsoid. The use of diamond-turning technology essentially solves that problem for aluminum and copper resonators. Accounting for the perturbing effect of ducts, microphones, and antennae has also been studied extensively.

Table 13 Uncertainty budget for determining the Boltzmann constant

Term	$u(k=1)$	$u(k=1)$ parts in 10^6 effect on k_B	Comment
Radius	nm on radius		
Microwave mode dispersion	4.5	0.18	Standard deviation of six modes using second-order theory of Mehl
Perturbation uncertainty	10	0.40	Based on measurements
Equivalence of microwave and acoustic volumes	50	2	Based on discrepancy between the microwave and replica estimates of the microphone volume
Temperature	mK		
Temperature calibration	0.3	1.10	Based on the agreement between the three thermometers
Temperature measurement uncertainty	0.25	0.92	This accounts for possible difference between the mean temperature of the gas and the temperature at the Equator
Correction to TPW		0.2	Effect of applying change in 2nd virial coefficient with temperature as a post correction
$M/\gamma 0$			
Isotopic mass		0.21	This is the uncertainty estimate from IRMM
Chemical impurity		1	This is difficult to estimate. We consider it unlikely that other noble gas impurities are at the limit of detectability
Zero pressure limit			
Analytical uncertainty		0.05	Based on the variation of results using different analytical schemes
Statistical uncertainty		0.04	Difference between shell compensated and non-compensated data
Acoustic perturbations			
Microphone compliance		0.1	Extrapolates to 0 (may account for dispersion of residuals in combined fits
Second-order shape perturbation		0.5	Uncertainty in applicability of models in imperfectly ellipsoidal quasisphere
Thermal boundary layer		1.4	As evidenced by negative 'excess' half-widths
Total (in quadrature)		3.09	

Two copper quasispheres manufactured by Paul Morantz and colleagues at the *Cranfield University Department of Precision Engineering* have recently been delivered to NPL. The spheres are nominally identical with an inner design surface given by Eq. 1 with a radius of 62 mm (volume $\sim$ 1 l) and characterized by $\varepsilon_1 = 0.001$ and $\varepsilon_2 = 0.0005$. Measurements with a coordinate measuring machine indicate that the deviation from form is less than $\pm 1.5\,\mu$m over the entire internal surface. We are confident that the closeness of this sphere to the ideal shape will ensure excellent consistency of microwave and acoustic data.

4.3 Microphones: Equivalent Volume Correction

Based on the studies of Mehl and Moldover [4], we expect the magnitude of the shape perturbation introduced by the microphones to be of the same order as the difference in volume between the case when the microphones are in place, and the perfect surface of the resonator with the microphones removed. Our results (§2.7) confirm this, however this correction is large, amounting to a correction of 11 parts in 10^6 in k_B for 2 GRAS 40BP or 40BF 0.64 cm (1/4 inch) microphones. The uncertainty in this correction is the largest contribution to our uncertainty budget (Table 13). For our next sphere we will use 0.32 cm (1/8 inch) microphones [GRAS 40 DP], which will produce a volume perturbation of $\sim$1 part in 10^6 in a sphere of volume 1 L. We expect to be able to correct for this with uncertainty well below 1 part in 10^6.

4.4 Isotopic Composition

As can be seen in Table 11, our two estimates of the zero pressure limit of c^2 in argon at 273.16 K differ by 2.7 parts in 10^6. Our initial analysis assumed that the isotopic composition of the gas was the same in the two experiments and we concluded that there was a difference of several parts in 10^6 between the results of the fixed and hung isotherms. Several weeks later when the gas sample from the second isotherm had been analysed at IRMM we found that the isotopic composition of the gas used on the 'hung' isotherm differed by 3.77 parts in 10^6 from the gas used on the 'fixed' isotherm which accounted for much of the difference in the speed of sound. We are continuing to study the variation in isotopic composition between nominally identical gas bottles. Our studies are not yet complete but indicate that our uncertainty estimates are sound.

4.5 Chemical Purity

With the exception of other noble gases, the SAES point-of-use purifiers should reduce the levels of all impurity gases to levels well below 1 part in 10^6. The impurity levels reported by suppliers do not refer to the level of other noble gases in argon, but informal conversations with the suppliers give us no reason to believe that there are significant levels of these gases in our argon. Our uncalibrated mass spectrometry

tests have identified only neon as a significant impurity. In addition, experiments with a cold trap held at a temperature of 100 K by one of us (LP) have confirmed that the levels of xenon and krypton make no detectable difference to the speed of sound.

In order to reduce this uncertainty we have begun preparation of specially prepared argon samples 'spiked' with known levels of other noble gases. We will use these to calibrate a gas chromatography/mass spectrometry measurement. We anticipate that detection levels of 0.3 part in 10^6 for helium and neon will be possible, which will reduce uncertainties substantially below 1 part in 10^6.

An alternative approach would be to use a gas other than argon. If we restrict ourselves to noble gases, the only practical possibility is helium, and there are several excellent reasons for using helium in this experiment. Use of helium with a point-of-use purifier and a cold-trap would solve the chemical impurity problem, however, it would raise many other experimental challenges.

4.6 Ducts

The gas inlet and outlet ducts on the sphere shift the frequencies of the resonance and a sensitivity analysis has shown that there is moderate sensitivity to the duct diameters and lengths. Recent theoretical and experimental study by Gillis et al. [34] support the validity of the models used to estimate this correction.

4.7 Volume/Equivalent Radius

The recent publication of the second-order shape corrections by Mehl [8], and the forthcoming publication of the effect of microwave probes by Underwood et al. [29], indicate that the uncertainty of the volume estimation using microwaves can be reduced to 0.3 parts in 10^6 in a quasi-spherical resonator of the correct form with a nominal radius of 50 mm. Preliminary measurements on a second quasi-sphere (TCU2) have been made and radius estimates from the 6 TM modes differ by less than ± 2 nm. The uncertainty in probe corrections and the equivalence of microwave and acoustic volumes increases this uncertainty, but it is still reasonable to expect that measurements in 62 mm radius spheres can be made with an uncertainty in k_B of less than 0.5 parts in 10^6.

Despite the robustness of the electromagnetic theory and the excellent agreement between modes, a pycnometric measurement of the volume will be a key step in establishing the resonator volume. Unfortunately we have found only one candidate liquid with which we can make low uncertainty measurements, namely water, and this has significant compatibility problems with copper. In order to overcome these problems, the copper must be coated with a 2 nm thick layer of benzotriazole (BTA) [35]. Using a separate 0.5 L copper sphere we have made four independent pycnometry measurements with results characterized by a range of volume of ± 1.3 parts in 10^6 which corresponds to ± 22 nm on the radius of the equivalent sphere. This would contribute 0.9 parts in 10^6 in uncertainty to an evaluation of k_B. A sphere coated with BTA will be used to confirm the determination of the volume determined by microwaves, but this

sphere will not be used for Boltzmann measurements because of the possible effects of contamination of the argon.

4.8 Acoustic Modelling

The resonator used in this study and the NPL-Cranfield resonator in which future measurements will be made have internal surfaces which are extremely close to the ideal triaxially ellipsoidal form. However, the *outer* surfaces of both resonators are far from being an ideal spherical shell. The outer surfaces have thickened regions for holding the resonators, clamping the hemispheres together, and attaching sensors of various kinds. This can lead to significant interactions between the radial acoustic modes used to determine k_B and the modes of vibration other than the 'breathing mode.' Critically, this can cause the sound pressure field of a nominally 'radial' acoustic mode to acquire a significant non-radial character. It may be that this feature is the one responsible for the pressure dependence of the excess half-width. Currently, finite element models can predict the frequency of radial modes in a perfectly spherical cavity with errors of less than 1 part in 10^6 [37], and investigations into more complex situations are ongoing.

4.9 Temperature

The calibration and use of the cSPRTs at the required level have proved much harder than originally anticipated. Many months of experiments have been spent for investigating the impact on calibration due to a wide range of possible factors, including many electrical effects. It is now clear that that a target uncertainty of ± 0.1 mK is achievable in practice, but only by using special procedures. In particular, the same bridge must be used to calibrate and measure the cSPRTs. In addition, the wiring used for the measurements must be identical with that used for calibration. Finally, two cSPRTs will be placed at each measurement location to ensure confidence.

The NPL-Cranfield resonator will be surrounded by an isothermal copper shield, and the reduction of the power from the acoustic preamplifier (§2.3, §2.5) should reduce thermal gradients to a fraction of a millikelvin. Gradients will be monitored by use of a 10-stage thermopile generating $400\,\mathrm{nV \cdot mK^{-1}}$.

4.10 Summary and Prospects

Considering the effects in §4.2 to §4.9, we have constructed a tentative uncertainty budget for our 2010 experiment (Table 14). The target of achieving an uncertainty of 1 part in 10^6 seems challenging, but achievable.

Table 14 Target uncertainty budget for determining the Boltzmann constant with NPL-Cranfield quasi-sphere

Term Radius	2009 $u(k = 1)$ (parts in 10^6 of k_B)	2010	Comment
Microwave mode dispersion	0.18	0.1	Larger sphere, better made and better understood
Perturbation uncertainty	0.40	0.2	Based on recent measurements
Equivalence of microwave and acoustic volumes	2	0.1	Smaller microphones
Temperature			
Temperature calibration	1.10	0.3	Use of same bridge and wiring in calibration and measurement
Temperature measurement	0.92	0.3	Much improved thermal design. Replacement of commercial acoustic amplifier with low power transimpedance amplifier
Correction to TPW	0.2	0.1	Improved temperature stability
$M/\gamma 0$			
Molar mass	0.21	0.21	Multiple measurements from each isotherm will confirm reproducibility and identify any systematic effects
Chemical impurity	1	0.5	Details uncertain, but will involve cold traps, gas chromatography and 'spiked' gas samples
Zero pressure limit			
Analytical uncertainty	0.05	0.05	Unlikely to change
Statistical uncertainty	0.04	0.1	Might increase with smaller microphones
Acoustic perturbations			
Microphone compliance	0.1	0.1	Extrapolates to 0 (may account for dispersion of residuals in combined fits
Second-order shape perturbation	0.5	0.1	Improved modeling and highly perfect form for resonator
Thermal boundary layer	1.4	0.5	Unknown, but we expect improvements in our general understanding
Total (in quadrature)	3.09	0.91	

Acknowledgments The authors would like to acknowledge the support and encouragement from many colleagues including but not limited to Richard Rusby, Gordon Edwards, Graham Machin, Leon Rogers, Daniel Truong, Arnaud Gillou, Roberto Gavioso and Paulo Alberto Giuliano Albo. We are grateful for the kind permission to use resonance-fitting software developed by Eric May. We gratefully acknowledge funding under the *Pathfinder* programme of the UK Department for *Business Innovation and Skills* and the EMRP programme of EU.

References

1. P.J. Mohr, B.N. Taylor, D.B. Newel, Rev. Mod. Phys. **80**, 633 (2008)
2. B. Felmuth, Ch. Gaiser, J. Fischer, Meas. Sci. Technol. **17**, R145 (2006)
3. M.R. Moldover, J.B. Mehl, M. Greenspan, J. Acoust. Soc. Am. **79**, 253 (1986)
4. M.R. Moldover, J.P.M. Trusler, T.J. Edwards, J.B. Mehl, R. Davis, J. Res. Natl. Bur. Stand. (U.S.) **93**, 85 (1988)
5. L. Pitre, M.R. Moldover, W.L. Tew, Metrologia **43**, 142 (2006)
6. G. Benedetto, R.M. Gavioso, R. Spagnolo, P. Marcarino, A. Merlone, Metrologia **41**, 74 (2004)
7. J.B. Mehl, M.R. Moldover, L. Pitre, Metrologia **41**, 295 (2004)
8. J.B. Mehl, Metrologia **46**, 554 (2009)
9. J.B. Mehl, J. Res. Natl. Inst. Stand. Technol. **122**, 163 (2007)
10. J.B. Mehl, M.R. Moldover, Phys. Rev. **A34**, 3341 (1986)
11. J.B. Mehl, M.R. Moldover, J. Chem. Phys. **74**, 4062 (1981)
12. C.A. Oxborrow, *The Effects of Geometry on Acoustic and Electromagnetic Resonances in a Spherical Cavity*, University of Delaware (1990)
13. NANOSHAPE s.a. Ultra Precision Machining, LIEGE Science Park, Rue Chasseurs Ardennais 1, B-4031 Angleur-Liège, Belgium
14. Tinsley Precision Instruments, http://www.tinsley.co.uk/
15. ASL Limited, http://www.aslltd.co.uk/
16. G.R.A.S. Sound & Vibration A/S, Skovlytoften 33, DK-2840 Holte, Denmark
17. SAES Getters, http://www.saesgetters.com/
18. Druck Pressure Meters, http://www.gesensing.com/druckproducts/
19. Air Products BIP Gases, http://www.airproducts.com/Products/SpecialtyGases/BIPGases/Default.htm
20. M. Varlam, S. Valkiers, M. Berglund, P. Taylor, R. Gonfiantini, P. De Bièvre, Int. J. Mass Spectrom. **269**, 71 (2008)
21. S. Valkiers, M. Varlam, M. Berglund, P. Taylor, R. Gonfiantini, P. De Bièvre, Int. J. Mass Spectrom. **269**, 78 (2008)
22. S. Valkiers, M. Varlam, K. Ruße, M. Berglund, P. Taylor, J. Wang, M. Milton, P. De Bièvre, Int. J. Mass Spectrom. **263**, 195 (2007)
23. S. Valkiers, M. Varlam, K. Ruße, M. Berglund, P. Taylor, J. Wang, M. Milton, P. De Bièvre, Int. J. Mass Spectrom. **264**, 10 (2007)
24. P. Taylor, S. Valkiers, P. De Bièvre, *Handbook of Stable Isotope Analytical Techniques*, vol. 1, chapter 1, ed. by P. de Groot (Elsevier, Amsterdam, 2006), pp. 759–787
25. M. Inkret, S. Valkiers, M. Berglund, P. Taylor, N. Majcen, J. Zupan, Acta Chim. Slov. **55**, 294 (2008)
26. Stanford Research Systems, http://www.thinksrs.com/
27. Krohn Hite, http://www.krohn-hite.com/
28. Labview, http://www.ni.com/labview/
29. R. Underwood, J.B. Mehl, L. Pitre, G.J. Edwards, G. Sutton, M. de Podesta, Meas. Sci. Technol. **7**, 075103 (2010)
30. *Repliset* supplied by Struers A/S, Pederstrupvej 84, DK-2750 Ballerup, Denmark
31. E.F. May, L. Pitre, J.B. Mehl, M.R. Moldover, J.W. Schmidt, Rev. Sci. Instrum. **75**, 3307 (2004)
32. C. Guianvar'h, R.M. Gavioso, G. Benedetto, L. Pitre, M. Bruneau, Rev. Sci. Instrum. **80**, 074901 (2009)
33. P. Gélat, N. Joly, M. de Podesta, G. Sutton, R. Underwood, *Acoustic Modelling in View of a Determination of the Boltzmann Constant Within 1 ppm for the Redefinition of the Kelvin*, AFPAC J. Phys.: Conference Series (2009)
34. K.A. Gillis, H. Lin, M.R. Moldover, J. Res. Natl. Inst. Stand. Technol. **114**, 5 (2009)
35. M.M. Antonijevic, M.B. Petrovic, Int. J. Electrochem. Sci. **3**, 1 (2008)

36. L. Pitre, Flow Effects in Quasispherical Resonators, presented at 4th Int. Conf. on Progress in Determining the Boltzmann Constant, Torino, Italy (2009)
37. A.R.H Goodwin, Ph.D. Thesis, University of London (1988)